PHYSICAL REVIEW A **85**, 053419 (2012)

Molecular above-threshold-ionization angular distributions with intense circularly polarized attosecond XUV laser pulses

Kai-Jun Yuan and André D. Bandrauk[*]

Laboratoire de Chimie Théorique, Faculté des Sciences, Université de Sherbrooke, Sherbrooke, Québec, Canada, J1K 2R1

(Received 10 February 2012; published 22 May 2012)

Photoionization of aligned and fixed nuclei three-dimensional $H_2{}^+$ and two-dimensional H_2 by intense circularly polarized attosecond extreme ultraviolet laser pulses is investigated from numerical solutions of the time-dependent Schrödinger equation. Molecular above-threshold-ionization angular distributions are found to be rotated with respect to the two laser perpendicular polarizations or, equivalently the symmetry axes of the molecule. The angle of rotation is critically sensitive to laser wavelength λ, photoelectron energy E_{en}, and molecular internuclear distance R. The correlated interaction of the two electrons in H_2 is shown to also influence such angular distribution rotations in different electronic states.

DOI: 10.1103/PhysRevA.85.053419 PACS number(s): 33.80.Rv, 42.65.Ky

I. INTRODUCTION

Rapid developments in laser pulse technology [1–3] provide the tools necessary for investigating electron dynamics on the attosecond (1 as $= 10^{-18}$ s) time scale. Such ultrashort laser pulses now offer the possibility of creating coherent electron wave packets inside molecules on the attosecond time scale and subnanometer size [4–6] and of probing the time-resolved transient structure of molecules, materials, and even biological systems via ultrafast electron diffraction [7,8]. "Illuminating" molecules from within with modern ultrafast attosecond lasers will allow the use of laser-induced electron diffraction (LIED) [9,10] for structural information which is encoded in interference patterns that result from the intrinsic wave nature of the electron and its laser-assisted scattering [11]. Such interference phenomena in diatomics have been predicted earlier by Cohen and Fano [12] and Kaplan and Markin [13] in direct perturbative single-photon ionization. This has been extended to nonperturbative photoionization with few-cycle intense laser pulses in LIED [9,14]. In these schemes, a laser-induced rescattering mechanism occurs at low frequency through recombination with the parent ion [15,16] or with neighboring ions for both linear [17] and circular polarizations [18] with electron wavelengths controlled by the laser intensity through laser-induced ponderomotive energies. The effects of orbital geometry on tunneling-rescattering ionization and the resulting interference have also been investigated in angular-resolved high-order molecular above-threshold-ionization (MATI) spectra [19]. This has been extended to circularly polarized pulses illustrating MATI angular distributions [20] and molecular high-order-harmonic generation [21] both at equilibrium and at large internuclear distance R.

Attosecond extreme ultraviolet (XUV) laser pulses have been used to compare the interference effects of the molecular orbital configurations of H_2 and $H_2{}^+$ in two-dimensional (2D) LIED for both linear and circular polarizations [22]. Ionization by attosecond XUV laser pulses produces a strong dependence on both the internuclear distance and the molecular orientation angle [23]. Most recently, Odenweller *et al.* [24] found that in tunneling ionizations of $H_2{}^+$ with 800-nm circularly polarized laser pulses, the photoelectron momentum angular distributions exhibited tilted (rotated) angles with respect to simple quasistatic model predictions. They attributed the unexpected momentum distributions to a complex electronic motion inside molecules at critical distances R_c [25,26], where enhanced ionization has previously been predicted to occur [27,28]. In atomic multiphoton ionization angular distributions, such asymmetry has also been observed with elliptically polarized 532- and 1064-nm laser pulses [29]. As pointed out by this work in atoms, asymmetry in ATI angular distributions is forbidden for circular polarization. The angular distributions were shown to be strongly dependent on the laser intensity, polarization, and electron energy contrary to atoms. Circularly polarized XUV laser pulse photoelectron angular distributions of H_2 were shown to exhibit slight rotations of angular distributions with respect to polarizations due to the helicity of the light [30,31].

In this paper we present numerical results which show that the rotation of three-dimensional (3D) $H_2{}^+$ and 2D H_2 angular distributions in photoionization with circularly polarized attosecond XUV laser pulses is a *general phenomenon* and is critically sensitive to the laser wavelength, photoelectron energy, internuclear distance, and symmetry of molecular orbitals. Simulations are performed for aligned $H_2{}^+$ by solving numerically the corresponding fixed nuclei time-dependent Schrödinger equation (TDSE). Attosecond photoionization processes in the weak-field regime can also be treated by perturbation theory methods [32]. For H_2 we use a reduced 2D model, restricting the electron motion in a plane with static nuclei, thus enabling to go beyond perturbation theory and independent of gauge transformations [33]. Such a fixed nuclei approach is appropriate due to the longer femtosecond time scale of nuclear motions. The attosecond XUV ultrashort laser pulses with frequency $\omega > I_p$ (I_p ionization potential), duration $T \leqslant 1.2$ fs, and intensity $I_0 = 1.0 \times 10^{14}$ W/cm^2 (3×10^{-3} a.u.) are adopted. Throughout this paper, atomic units (a.u.) $e = \hbar = m_e = 1$ are used unless otherwise stated.

II. NUMERICAL METHODS

The TDSE for a fixed nuclei prealigned molecular ion $H_2{}^+$ is appropriately written with respect to the center of mass of

---

[*] andre.bandrauk@usherbrooke.ca

two protons at position $\pm R/2$ as

$$i\frac{\partial}{\partial t}\psi(\mathbf{r},t) = \left[-\frac{1}{2}\nabla^2 + V_{\text{en}}(\mathbf{r}) + V_L(\mathbf{r},t)\right]\psi(\mathbf{r},t), \quad (1)$$

where ∇^2 is the Laplacian on the right-hand side of Eq. (1). The 3D TDSE is described using cylindrical coordinates (ρ,θ,z) with $(x = \rho\cos\theta,\ y = \rho\sin\theta)$, where the radial and angular variables are easily separated. (x,y) is the molecular plane with the x axis along the internuclear distance. We can also reduce the 3D problem to 2D by separating the perpendicular z coordinate. 2D calculations are also well suited for circularly polarized laser pulses which confine electrons in the plane of molecules.

The laser-electron radiative coupling is described by the time-dependent potential

$$V_L(\rho,\theta,t) = \hat{e}_x\rho\cos\theta E_x(t) \pm \hat{e}_y\rho\sin\theta E_y(t) \quad (2)$$

in the length gauge for a one-color laser pulse,

$$\mathbf{E}(t) = \hat{e}_x E_0 f(t)\cos(\omega t) \pm \hat{e}_y E_0 f(t)\sin(\omega t), \quad (3)$$

where $\hat{e}_{x/y}$ is the polarization direction for left-hand $(+)$ and right-hand $(-)$ circular polarizations. A smooth pulse envelope $f(t) = \sin^2(\pi t/T)$ with time duration $T = 6\tau$ $(1\tau = 2\pi/\omega$, 1 optical cycle) and maximum amplitude E_0 for intensity $I_0 = \frac{1}{2}c\varepsilon_0 E_0^2$ is adopted. The TDSE is solved numerically by a second-order split-operator method in the time step δt combined with a fifth-order finite difference method and Fourier transform technique in the spatial steps $\delta\rho$, $\delta\theta$, and δz [34,35]. The time step is taken to be $\delta t = 0.01$ a.u. $= 0.24$ as, the spatial discretization is $\delta\rho = \delta z = 0.25$ a.u. for radial grid ranges $0 \leqslant \rho \leqslant 128$ a.u., $|z| \leqslant 64$ a.u., and the angle grid size $\delta\theta = 0.025$ radian. To prevent unphysical effects due to the reflection of the wave packet from the boundary, we multiply $\psi(\rho,\theta,z,t)$ by a "mask function" or absorber in the radial coordinate with the form $\cos^{1/8}[\pi(\rho - \rho_{\text{a}})/2\rho_{\text{abs}}]$ [36]. For all results reported here we set the absorber domain $\rho_{\text{a}} = \rho_{\max} - \rho_{\text{abs}} = 104$ a.u. with $\rho_{\text{abs}} = 24$ a.u., exceeding well the field-induced electron oscillation $\alpha_d = E_0/\omega^2$ of the electron.

An energy analysis of the ionization probabilities is employed based on a Fourier analysis of the associated flux [electron current density $\mathcal{J}(\theta,t)$] to describe photoelectron angular distributions [22] after integrating out z perpendicular to the (x,y) molecular plane, i.e., averaged over z. The corresponding time-independent energy-resolved angular differential yield (photoelectron spectra) is obtained by a Fourier transform:

$$\mathcal{J}(\theta,E) \sim \int e^{-iEt}\mathcal{J}(\theta,t)dt, \quad (4)$$

where $E = p^2/2$ is the kinetic energy of an ionized electron with wave vector $k = p = 2\pi/\lambda_e$ (in a.u.), p is the momentum, and λ_e is wavelength. The angular distributions $\mathcal{J}^{E_{\text{en}}}(\theta)$ at photoelectron kinetic energies $E_{\text{en}} = n\omega - I_p$ corresponding to n-order multiphoton ionizations are obtained by integrating over energy in Eq. (4),

$$\mathcal{J}^{E_{\text{en}}}(\theta) = \int_{E_{\text{en}}-\omega/2}^{E_{\text{en}}+\omega/2} dE\,\mathcal{J}(\theta,E). \quad (5)$$

III. RESULTS AND DISCUSSIONS

We first consider photoionization of $H_2{}^+$. Figures 1 through 4 show the results of MATI angular distributions $\mathcal{J}^{E_{\text{en}}}(\theta)$ at particular photoelectron kinetic energies E_{en} for the $H_2{}^+$ ground $1s\sigma_g$ electronic state at different internuclear distance R in ultrashort intense left-hand and right-hand circularly polarized XUV laser pulses with varying wavelengths λ (angular frequency $\omega = 2\pi c/\lambda$). The corresponding electron wavelengths λ_e (in a.u.) obtained from $n\omega = I_p + 2\pi^2/\lambda_e^2$ are displayed in Table I. The Keldysh parameter $\gamma = \sqrt{I_p/2U_p} \geqslant 20 \gg 1$ indicating multiphoton ionization processes [1]. From Figs. 1 through 4 we see that the structure of the angular distributions is critically sensitive to the photon angular frequency ω, photoelectron kinetic energy E_{en} (MATI peaks), and internuclear distance R. We also illustrate in Fig. 5 the corresponding electron density $\mathcal{P}_{\text{ex}}(t) = |\psi_{\text{ex}}(t)|^2$ at time $t = 4\tau$ of the total excited-ionized wave function defined as [37]

$$\psi_{\text{ex}}(t) = \psi(t) - \langle\psi(t=0)|\psi(t)\rangle\psi(t=0). \quad (6)$$

For comparison, in Fig. 2 we also display, the equilibrium $H_2{}^+$ results using a reduced 2D model [22]. It is found that both the 3D (Fig. 1) and 2D (Fig. 2) models show essentially identical results, thus indicating that the reduced 2D calculations can give an adequate description of the XUV photoionization processes at high intensities. Therefore as shown in Fig. 6 for the two-electron system H_2 we use reduced 2D models to describe the photoionization processes in circularly polarized XUV laser fields.

For the photoionization of equilibrium $H_2{}^+$ in Fig. 1, we note that the MATI angular distributions at photoelectron wavelengths $\lambda_e > R_e = 2$ a.u. (low photoelectron energy $E_{\text{en}} < 2\pi^2/R_e^2$) rotate anticlockwise and clockwise, for left-hand and right-hand circularly polarized laser pulses, i.e., following the direction of field polarizations. This is mainly due to the helicity of the ionizing photons [30,31]. The rotation angle of the angular distributions decreases as the laser wavelength λ decreases since higher-energy electrons with shorter wavelengths are created, thus diminishing the effects of Coulomb potentials. For example, as shown in Fig. 1(a), the rotation angle for the one-photon $\lambda = 40$ nm ionization at E_{e1} is approximately 15° with respect to the polarization direction perpendicular to the molecular axis. In the case of $\lambda = 20$ nm in Fig. 1(d), the angle decreases to 7.5° and for $\lambda = 10$ nm, the angle nodes nearly lie along the perpendicular polarization axis. Similar results occur for the two-photon ionization at E_{e2}. At $\lambda = 40$ nm the rotation angle from the molecular axis is about 25° in Fig. 1(b) and 15° at $\lambda = 20$ nm in Fig. 1(e). For the photoelectron angular distribution at energies $E_{\text{en}} > 2\pi^2/R_e^2$ $(\lambda_e < R_e)$, more nodes are produced and the rotation of angular distributions gradually disappears. In Figs. 1(f), 1(h), and 1(i), the angular distributions are essentially identical for left-hand and right-hand circular polarizations. Moreover, we note that the intensity of the parallel (to the molecular axis) ionization relative to the perpendicular case also increases with laser wavelength λ, i.e., with lower ionized electron energies, thus reflecting the increasing role of the Coulomb potential.

We adopt a $\delta(t)$ pulse ultrafast ionization model of two-center problems to understand the sensitivity of the rotation of

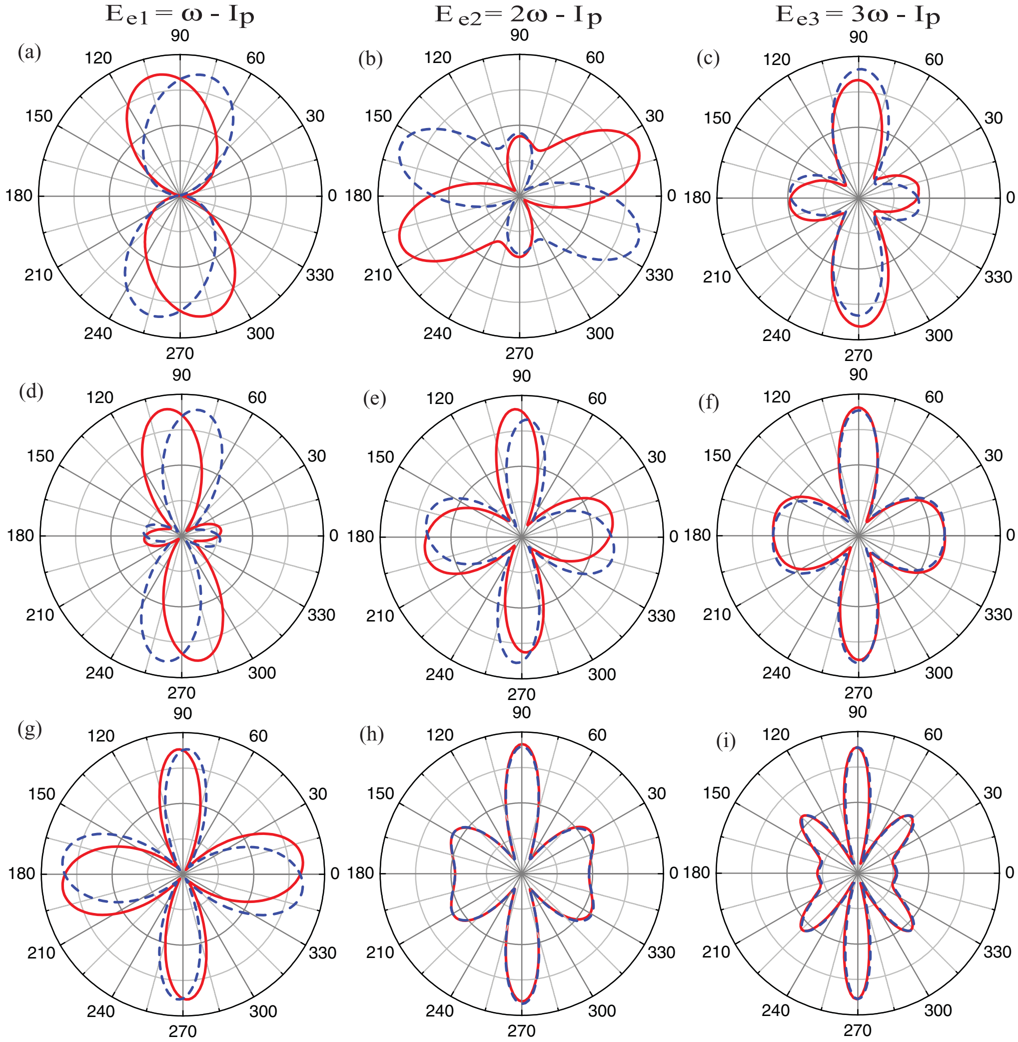

FIG. 1. (Color online) MATI angular distributions $\mathcal{J}^{E_{\rm en}}(\theta)$ at photoelectron energies $E_{\rm en}$ for 3D $H_2{}^+$ at $R_e = 2$ a.u. in left-hand (solid line) and right-hand (dashed line) circularly polarized XUV laser pulses with wavelengths $\lambda = 40$ nm [upper row, (a)–(c)], 20 nm [middle row, (d)–(f)], and 10 nm [bottom row, (g)–(i)], and intensity $I_0 = 1.0 \times 10^{14}$ W/cm^2 (3.0×10^{-3} a.u.).

the MATI angular distributions to photoelectron energies $E_{\rm en}$. The corresponding angular distribution amplitude of the photoelectron ionization is given by Fourier transform of the molecular wave function $\psi(t = 0^+)$, and can be expressed as [9]

$$f(\mathbf{p}) = \sqrt{2}\cos[(\mathbf{F} + \mathbf{p}) \cdot \mathbf{R}/2]\psi(|\mathbf{F} + \mathbf{p}|), \tag{7}$$

where $\mathbf{p}$ and $\mathbf{F}$ are the momentum vector of the photoelectron and the pulse field amplitude, respectively. The electron wave function after the interaction with the $\delta(t)$ pulse is given by $\psi(t = 0^+) = \exp(-i\mathbf{F} \cdot \mathbf{r})\psi_{1\sigma_g}$ with the initial electron state of $H_2{}^+$ at internuclear distance R before the interaction $\psi_{1\sigma_g} = [\psi_{1s}(-\mathbf{R}/2) + \psi_{1s}(\mathbf{R}/2)]/\sqrt{2}$, i.e., a linear combination of hydrogenic $1s$ orbitals located at $\pm\mathbf{R}/2$. One sees that the effect of an ultrashort pulse, approaching a $\delta(t)$ function pulse, will be to shift simply the total momentum distributions of the constituent atomic orbitals of molecular orbitals by the field amplitude $\mathbf{F}$ and this is multiplied by the two center interference phase function. In the present model, $\mathbf{F} \approx 0$ in Eq. (7) since at laser intensity $I_0 = 1 \times 10^{14}$ W/cm^2 (3.0×10^{-3} a.u.) and field amplitude $E_0 = 0.053$ a.u. the ponderomotive energies $U_p = E_0^2/4\omega^2 \ll I_p$ and the Stark potential energy $\pm FR/2$ is negligible compared to the phase $pR/2$.

In Fig. 1 we see that for the case $\lambda_e > R_e$, since $\cos(\mathbf{p} \cdot \mathbf{R}/2) = \cos(pR\cos\vartheta/2)$, then $pR/2 = \pi R/\lambda_e < \pi$, where

TABLE I. Wavelengths λ_e (a.u.) of the ionized electron at specific MATI energies $E_{\rm en}$ for $H_2{}^+$ at different R in circularly polarized XUV laser pulses with varying wavelengths λ.

R (a.u.)	$E_{\rm en}$	$\lambda = 10$ nm	20 nm	40 nm	60 nm
$R_e = 2$	E_{e1}	2.39	4.09	22.2	
	E_{e2}	1.57	2.39	4.09	
	E_{e3}	1.25	1.85	2.92	
$R_c = 7$	E_{e1}	2.28			39.0
	E_{e2}	1.54			5.06
	E_{e3}	1.24			3.59
$R_d = 15$	E_{e1}	2.25			14.0
	E_{e2}	1.53			4.79
	E_{e3}	1.23			3.49

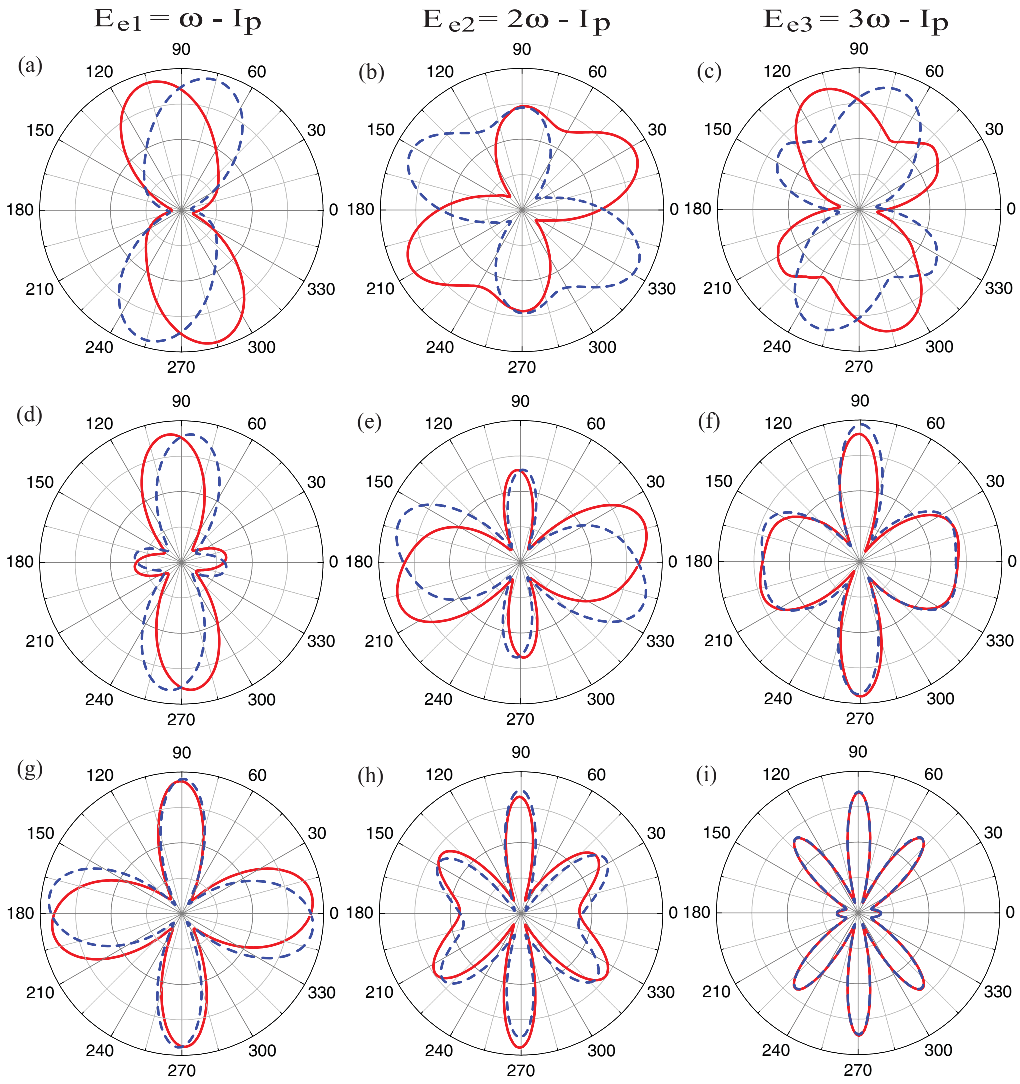

FIG. 2. (Color online) MATI angular distributions $\mathcal{J}^{E_{\rm en}}(\theta)$ at photoelectron energies $E_{\rm en}$ for reduced 2D $H_2{}^+$ at $R_e = 2$ a.u. in left-hand (solid line) and right-hand (dashed line) circularly polarized XUV laser pulses with wavelengths $\lambda = 40$ nm [upper row, (a)–(c)], 20 nm [middle row, (d)–(f)], and 10 nm [bottom row, (g)–(i)], and intensity $I_0 = 1.0 \times 10^{14}$ W/cm^2 (3.0×10^{-3} a.u.).

ϑ is the angle between the momentum of the ejected electron and the molecular axis, no diffraction is possible. The circular polarization angular distributions are simply superpositions of the linear parallel and perpendicular polarizations [22,38]. As shown in Fig. 5(a), under such a condition most of the electron wave packet with classical momentum $p = \sqrt{2(n\omega - I_p)}$ drifts away from the nuclei at an angle with respect to the laser polarizations, and then rapidly ionizes. Therefore, rotation occurs in the final angular distributions due to the two-center nonspherical Coulomb potential. The departure angle depends on the rotation of the circularly polarized XUV laser fields. For left-hand and right-hand circular polarizations, the angular distributions show complete up-down symmetry, indicating the effects of helicity of the light on the rotation. Of note is that due to effects of the proton Coulomb potential and scattering of electron wave packets, the rotation angles of parallel and perpendicular electron distributions are not the same.

As laser wavelengths λ decrease, energies $E_{\rm en} = p^2/2 = n\omega - I_p$ (in a.u.) increase and the corresponding electron wavelengths $\lambda_e = 2\pi/p$ decrease. The two-center interference is enhanced gradually. At $\lambda_e < R_e$, the final angular distributions mainly result from double-slit electron diffraction of the continuum electron wave packet. As shown in Fig. 5(b) striking classical Young double-slit interference stripes are observed. This has been previously assigned to the contributions of large $l \geqslant 3$ angular momentum states [39,40] due to strong deviation from spherical symmetry of the electron continuum wave functions. Thus as seen in Figs. 5(d)–5(f), diffraction patterns increase with increasing R. As a result the multiple "wings" as predicted in Eq. (7) appear in the angular distribution, and the rotation due to helicity of the circularly polarized XUV laser pulses vanishes, as confirmed from the identical angular distributions for left-hand and right-hand circular polarizations in Figs. 1(f), 1(h), and 1(i). At high photoelectron energy $E_{\rm en}$ and shorter electron wavelengths $\lambda_e < R_e$, the effects of molecular geometry and orientation on the ionization rate [23] become weaker, thus the intensity of the parallel nodes increases, as shown in Fig, 1.

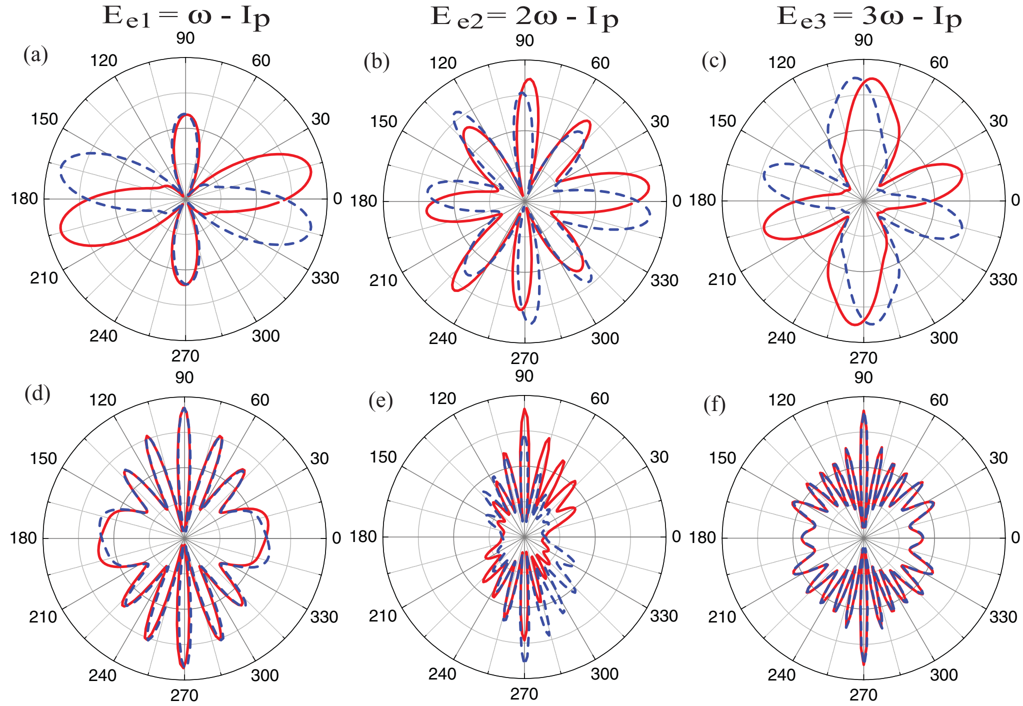

FIG. 3. (Color online) MATI angular distributions $\mathcal{J}^{E_{\rm en}}(\theta)$ at photoelectron energies $E_{\rm en}$ for 3D H_2^+ at $R_c = 7$ a.u. in left-hand (solid line) and right-hand (dashed line) circularly polarized XUV laser pulses with wavelengths $\lambda = 60$ nm (upper row) and 10 nm (bottom row), and intensity $I_0 = 1.0 \times 10^{14}$ W/cm^2 (3.0×10^{-3} a.u.).

At large internuclear distance R, the rotation of the MATI angular distribution can also be observed at $\lambda_e < R$. In Figs. 3 and 4 we, respectively, display the results of H_2^+ at the charge resonance enhanced ionization (CREI) internuclear distance $R_c = 7$ a.u. [27,28] and at the large dissociation distance $R_d = 15$ a.u. The photoelectron angular distributions of the

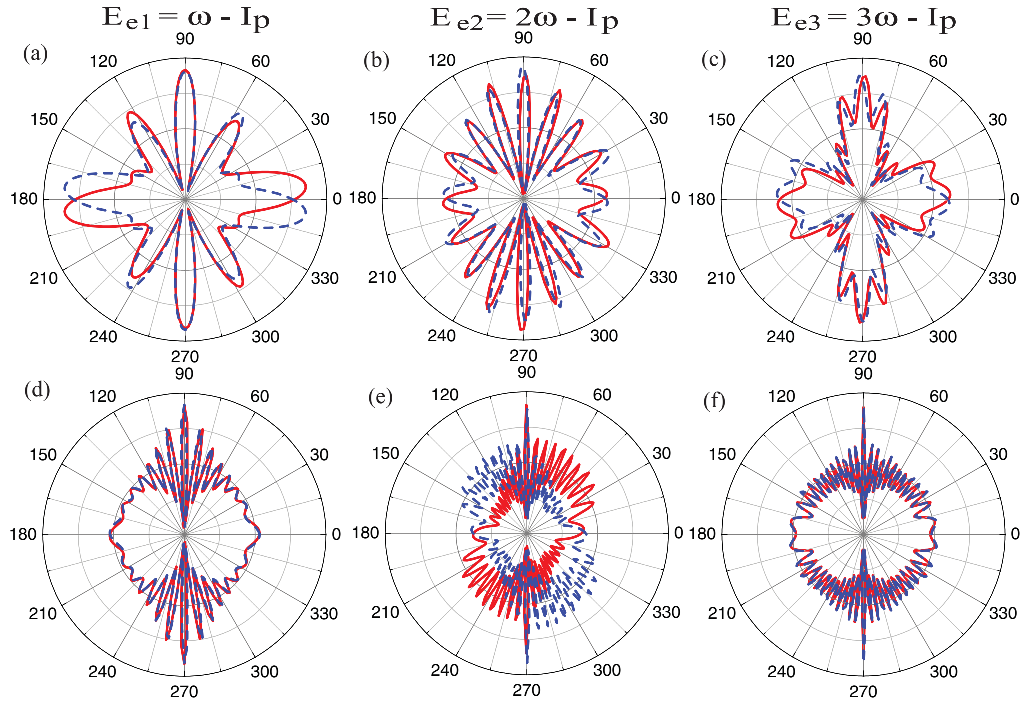

FIG. 4. (Color online) MATI angular distributions $\mathcal{J}^{E_{\rm en}}(\theta)$ at photoelectron energies $E_{\rm en}$ for 3D H_2^+ at $R_d = 15$ a.u. in left-hand (solid line) and right-hand (dashed line) circularly polarized XUV laser pulses with wavelengths $\lambda = 60$ nm (upper row) and 10 nm (bottom row), and intensity $I_0 = 1.0 \times 10^{14}$ W/cm^2 (3.0×10^{-3} a.u.).

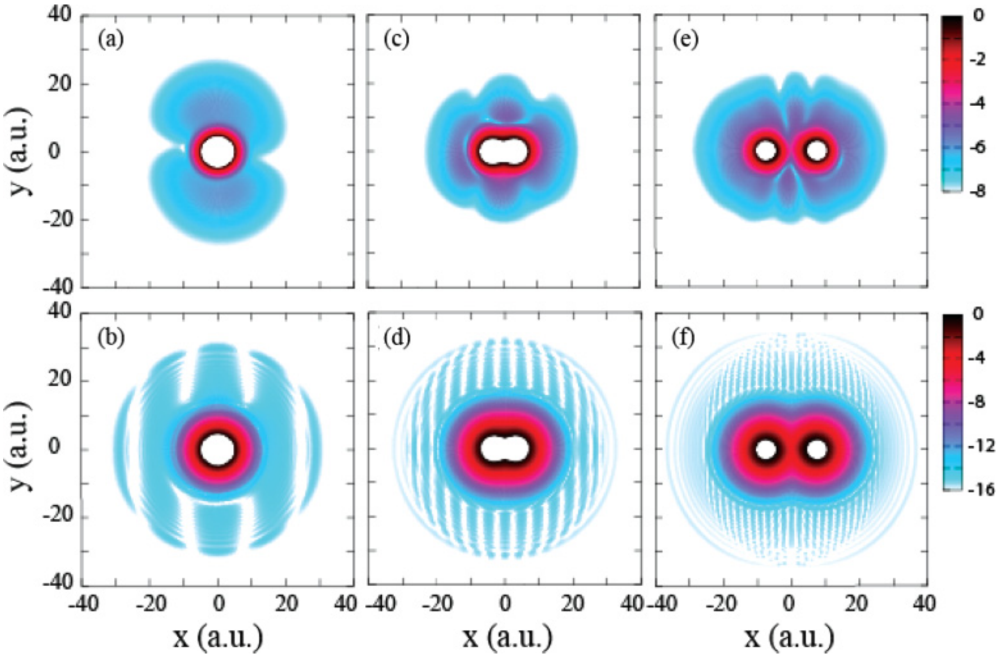

FIG. 5. (Color online) Ionized probability $\mathcal{P}_{ex}(x,y)$ distributions for 3D $H_2{}^+$ at time $t = 4\tau$ at different internuclear distances $R_e = 2$ a.u. [(a) and (b)], $R_c = 7$ a.u. [(c) and (d)], and $R_d = 15$ a.u. [(e) and (f)], for left-hand circularly polarized XUV laser pulses with wavelengths $\lambda = 40$ nm (a), $\lambda = 60$ nm [(c) and (e)], and $\lambda = 10$ nm [(b), (d), and (f)], and intensity $I_0 = 1.0 \times 10^{14}$ W/cm^2 (3.0×10^{-3} a.u.).

first three MATI peaks are illustrated for circularly polarized XUV laser pulses with long $\lambda = 60$ nm and short 10 nm photon wavelengths. However, we note that in Figs. 3(b), 3(c), and 4(a)–4(c) at $\lambda_e < R_c$ with striking diffraction "wings," the rotation of the angular distributions in parallel and perpendicular polarizations is also observed. As illustrated in Figs. 5(c) and 5(e), an increase of internuclear distance R decreases the ionization potential I_p and the amplitude of the two-center interference, leading to increase of direct ionizations and decrease of LIED effects. As a consequence, the angular distribution rotation appears as well. Comparing with Fig. 3 at the CREI distance $R_c = 7$ a.u., Fig. 4 at large dissociation distance $R_d = 15$ a.u. shows small rotation of angular distributions due to weaker Coulomb potentials. At larger R in Figs. 3(d), 3(e), 4(b), and 4(c) the major angular distribution does not follow the laser polarization due to molecular Coulomb potential altering the relative intensity of the nodes as a result of LIED. At high photoelectron energy E_{e3}, angular distribution rotation vanishes for both internuclear distances $R_c = 7$ a.u. and $R_d = 15$ a.u., reflecting the decrease of Coulomb potential. As shown in Figs. 3(f), 4(f), 5(d), and 5(f), clear double-slit interference and LIED patterns are produced with $R\cos\theta \sim \lambda_e$.

Similar results of angular distribution rotations have also been obtained for $H_2{}^+$ in tunneling ionization, where the Keldysh parameter $\gamma \sim 1$. As we have shown previously [20] with $\lambda = 400$ nm and $I_0 = 2 \times 10^{14}$ W/cm^2 (6.0×10^{-3} a.u.) circularly polarized laser pulses, equilibrium MATI angular distributions at the cutoff energies $E_e = 8U_p$ exhibit a rotation with respect to polarizations directions. However, at extended large internuclear distance $R = 22$ a.u. where collisions of the ionized electron with neighboring ions occur resulting in LIED patterns with multiple "wings," such angular distribution rotation with respect to laser polarization directions nearly disappears due to weaker effects of Coulomb potentials. At the critical internuclear distance $R_c = 7$ a.u., rotations are also obtained due to enhanced ionization resulting in intramolecular electron motions [24]. Recent experiments in H_2 circularly polarized 800-nm laser ionization also show anomalous angular distributions [41]. Therefore we see that the rotation of angular distributions with respect to circular polarization axes is a general phenomenon and is sensitive to the photoelectron kinetic energy.

Finally, in Fig. 6 we show photoelectron angular distributions at energies $E_{e1} = \omega - I_p$ in the 2D H_2 $X\,{}^1\Sigma_g^1$, $A\,{}^3\Sigma_u^+$, and $B\,{}^1\Sigma_u^+$ electronic states [22] at equilibrium R_e by left-hand circularly polarized attosecond XUV laser pulses, as used for $H_2{}^+$ but with different wavelengths λ. We only show the results of photoelectron wavelengths $R_e < \lambda_e < 2R_e$. The laser wavelengths are $\lambda = 15$ nm (upper row), 10 nm (middle row), and 7.5 nm (bottom row). Again the laser wavelength λ dependent rotation of angular distributions is obtained. The similar results of angular distribution rotations should occur as $H_2{}^+$ in Figs. 1 through 5 for higher-order MATI spectra. However, we note that such rotations are also sensitive to molecular orbital configurations. The correlated interaction of the two electrons in H_2 clearly influences the rotations. For the ground $X\,{}^1\Sigma_g^1$ electronic states with molecular orbital configuration $1\sigma_g(1)1\sigma_g(2)$ in Figs. 6(a), 6(d), and 6(g) no rotations of angular distributions with respect to the perpendicular polarization occurs for both wavelengths, whereas for the excited $A\,{}^3\Sigma_u^+$ [Figs. 6(b), 6(e), and 6(h)] and $B\,{}^1\Sigma_u^+$ [Fig. 6(c), 6(f), and 6(i)] states with $1\sigma_g(1)1\sigma_u(2) - 1\sigma_g(2)1\sigma_u(1)$ and $1\sigma_g(1)1\sigma_u(2) + 1\sigma_g(2)1\sigma_u(1)$ orbital configurations, the rotation angle decreases as laser wavelength λ decreases. Moreover, the rotation angle in the $B\,{}^1\Sigma_u^+$ state is larger than

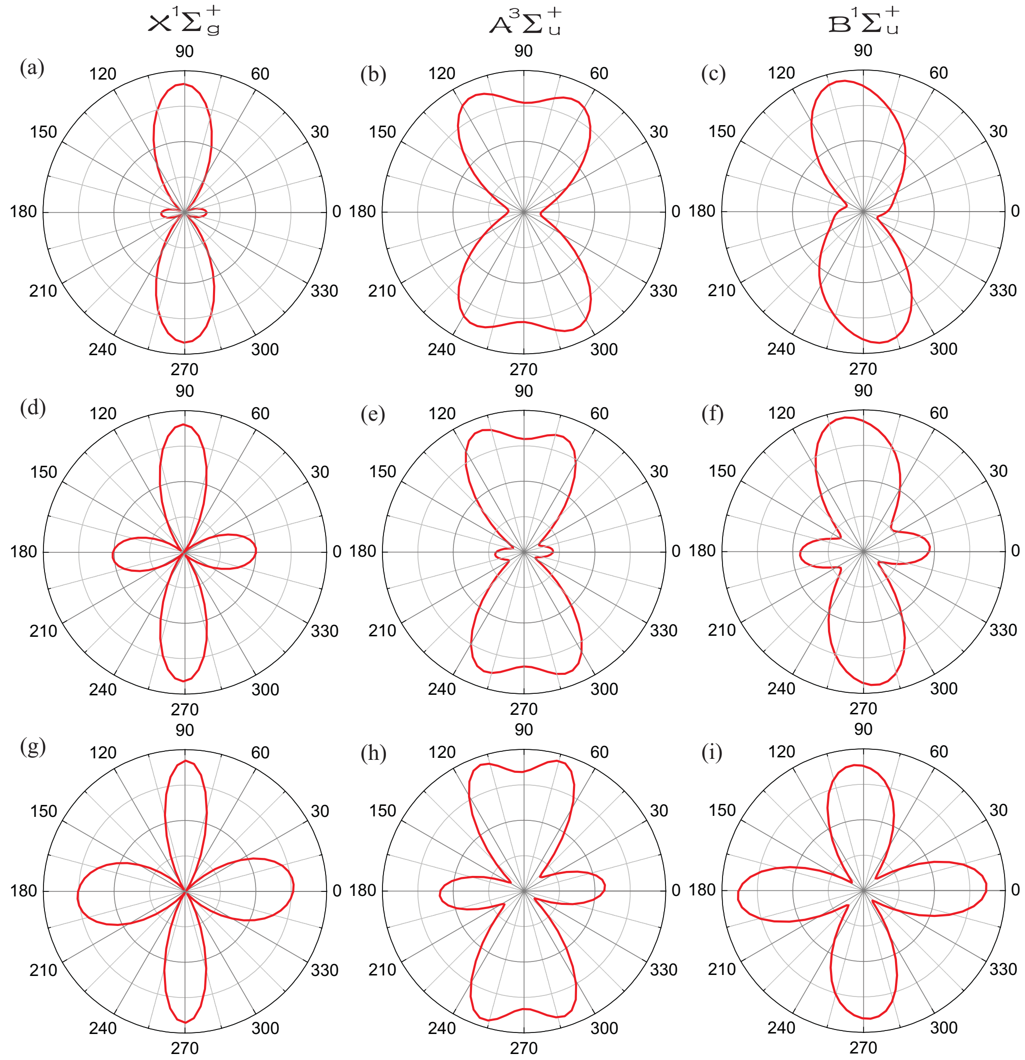

FIG. 6. (Color online) Angular distributions at kinetic energies E_{e1} for the 2D H_2 $X\ ^1\Sigma_g^1$, $A\ ^3\Sigma_u^+$, and $B\ ^1\Sigma_u^+$ electronic states at R_e in left-hand circularly polarized XUV laser pulses with wavelengths $\lambda = 15$ nm (upper row), 10 nm (middle row), and 7.5 nm (bottom row), and intensity $I_0 = 1.0 \times 10^{14}$ W/cm^2 (3.0×10^{-3} a.u.).

that in the $A\ ^3\Sigma_u^+$ state, reflecting the effects of the symmetry of molecular orbitals.

From Fig. 6 we also see that relative intensities of parallel and perpendicular (to the molecular axis) angular distributions are critically sensitive to laser and photoelectron wavelengths for the three H_2 electronic states. At $\lambda = 15$ nm, the perpendicular distributions dominate. As photon energies ω increase, i.e., photoelectron wavelengths λ_e decrease, the parallel distributions in intensity increase as well. At $\lambda = 7.5$ nm, the parallel and perpendicular distributions are comparable. The laser wavelength and photoelectron kinetic energy dependence of parallel and perpendicular distribution intensities mainly result from the effects of the electronic charge clouds associated with each scattering center in the photoelectron ionization processes. Thus such nonspherical Coulomb potential leads to orientation-dependent ionization rates [33], which allow for tomographic imaging of molecular orbitals [10]. Of note is that at $\lambda = 7.5$ nm, the parallel and perpendicular distributions for the $X\ ^1\Sigma_g^1$ and $B\ ^1\Sigma_u^+$ states are nearly equivalent, whereas for the $A\ ^3\Sigma_u^+$ state the perpendicular distributions are still dominant. This can be attributed to the effects of the electron configurations on the orientation-dependent ionization rate.

IV. CONCLUSIONS

MATI angular distributions are reported for H_2^+ at different internuclear distance R produced by attosecond intense XUV laser pulses. Such ultrashort laser pulses allow for measurement of multiphoton processes for fixed nuclei molecular configurations. Numerical solutions of the appropriate TDSE's for MATI processes allow for obtaining gauge invariant, nonperturbative angular distributions for different photon wavelengths λ and internuclear distance R. It is found that MATI angular distributions from circularly polarized XUV laser pulses exhibit asymmetries characterized by rotations of angular distributions with respect to the symmetry axes of the H_2^+ molecular ion. These molecular asymmetries which are absent in atomic ATI spectra generated by circularly polarized laser pulses [29] reflect the angular dependent ionization rates. These are presented for ultrashort intense laser pulse ionization at long wavelength, 400 nm [20], and are shown to be present also for short wavelength XUV multiphoton ionization. XUV wavelengths offer also the possibility of observing LIED [9,10] as photoelectron wavelengths become shorter than the internuclear distance R. MATI angular distributions remain rotated in the presence of LIED effects. 2D simulations for the two-electron H_2 molecule confirm that rotation of MATI angular distributions are also sensitive to electron configurations and XUV ionization wavelengths.

ACKNOWLEDGMENTS

We thank RQCHP and Compute Canada for access to massively parallel computer clusters and CIPI (Canadian Institute for Photonic Innovations) for financial support of this research in its ultrafast science program.

---

[1] T. Brabec and F. Krausz, Rev. Mod. Phys. **72**, 545 (2000).
[2] F. Krausz and M. Ivanov, Rev. Mod. Phys. **81**, 163 (2009).
[3] Z. Chang and P. Corkum, J. Opt. Soc. Am. B **27**, B9 (2010).
[4] S. Chelkowski, G. L. Yudin, and A. D. Bandrauk, J. Phys. B **39**, S409 (2006).
[5] H. Niikura, D. M. Villeneuve, and P. B. Corkum, Phys. Rev. Lett. **94**, 083003 (2005).
[6] H. C. Shao and A. F. Starace, Phys. Rev. Lett. **105**, 263201 (2010).
[7] T. Morishita, A. T. Le, Z. Chen, and C. D. Lin, Phys. Rev. Lett. **100**, 013903 (2008); New J. Phys. **10**, 025011 (2008).
[8] M. Peters, T. T. Nguyen-Dang, C. Cornaggia, S. Saugout, E. Charron, A. Keller, and O. Atabek, Phys. Rev. A **83**, 051403(R) (2011).
[9] T. Zuo, A. D. Bandrauk, and P. B. Corkum, Chem. Phys. Lett. **259**, 313 (1996).
[10] M. Meckel, D. Comtois, D. Zeidler, A. Staudte, D. Pavicic, H. C. Bandulet, H. Pépin, J. C. Kieffer, R. Dörner, D. M. Villeneuve, and P. B. Corkum, Science **320**, 1478 (2008).
[11] M. J. J. Vrakking, Physics **2**, 72 (2009).
[12] H. D. Cohen and U. Fano, Phys. Rev. **150**, 30 (1966).
[13] I. G. Kaplan and A. P. Markin, Sov. Phys. Dokl. **14**, 36 (1969).
[14] S. X. Hu and L. A. Collins, Phys. Rev. Lett. **94**, 073004 (2005).
[15] P. B. Corkum, Phys. Rev. Lett. **71**, 1994 (1993).
[16] A. D. Bandrauk, S. Chelkowski, and S. Goudreau, J. Mod. Opt. **52**, 411 (2005).
[17] A. D. Bandrauk, S. Chelkowski, H. Yu, and E. Constant, Phys. Rev. A **56**, R2537 (1997); A. D. Bandrauk, S. Barmaki, and G. L. Kamta, Phys. Rev. Lett. **98**, 013001 (2007).
[18] A. D. Bandrauk, S. Chelkowski, and K. J. Yuan, Int. Rev. At. Mol. Phys. **2**, 1 (2011).
[19] M. Okunish, R. Itaya, K. Shimada, G. Prümper, K. Ueda, M. Busuladžić, A. Gazibegović-Busuladžić, D. B. Milošević, and W. Becker, Phys. Rev. Lett. **103**, 043001 (2009).
[20] K. J. Yuan and A. D. Bandrauk, Phys. Rev. A **84**, 013426 (2011).
[21] K. J. Yuan and A. D. Bandrauk, Phys. Rev. A **81**, 063412 (2010); **83**, 063422 (2011); **84**, 023410 (2011).
[22] K. J. Yuan, H. Z. Lu, and A. D. Bandrauk, Phys. Rev. A **80**, 061403(R) (2009); **83**, 043418 (2011).
[23] S. Selstø, M. Førre, J. P. Hansen, and L. B. Madsen, Phys. Rev. Lett. **95**, 093002 (2005).
[24] M. Odenweller, N. Takemoto, A. Vredenborg, K. Cole, K. Pahl, J. Titze, L. P. H. Schmidt, T. Jahnke, R. Dörner, and A. Becker, Phys. Rev. Lett. **107**, 143004 (2011).
[25] N. Takemoto and A. Becker, Phys. Rev. Lett. **105**, 203004 (2010); Phys Rev. A **84**, 023401 (2011).
[26] F. He, A. Becker, and U. Thumm, Phys. Rev. Lett. **101**, 213002 (2008).
[27] T. Zuo and A. D. Bandrauk, Phys. Rev. A **52**, R2511 (1995); S. Chelkowski and A. D. Bandrauk, J. Phys. B **28**, L723 (1995).
[28] T. Seideman, M. Y. Ivanov, and P. B. Corkum, Phys. Rev. Lett. **75**, 2819 (1995).
[29] M. Bashkansky, P. H. Bucksbaum, and D. W. Schumacher, Phys. Rev. Lett. **59**, 274 (1987); **60**, 2458 (1988).
[30] D. Akoury *et al.*, Science **318**, 949 (2007).
[31] A. H. Kreidi *et al.*, Phys. Rev. Lett. **100**, 133005 (2008).
[32] M. V. Frolov, N. L. Manakov, A. A. Silaev, N. V. Vvedenskii, and A. F. Starace, Phys. Rev. A **83**, 021405(R) (2011).
[33] G. L. Kamta and A. D. Bandrauk, Phys. Rev. A **71**, 053407 (2005).
[34] A. D. Bandrauk and H. Z. Lu, in *High-Dimensional Partial Differential Equations in Science and Engineering*, edited by A. D. Bandrauk, M. Delfour, and C. LeBris, CRM Lecture Series, Vol. 41 (American Mathematical Society, Philadelphia, 2007), pp. 1–15.
[35] A. D. Bandrauk and H. Shen, J. Chem. Phys. **99**, 1185 (1993).
[36] F. He, C. Ruiz, and A. Becker, Phys. Rev. A **75**, 053407 (2005).
[37] A. D. Bandrauk, J. Manz, and K. J. Yuan, Laser Phys. **19**, 1559 (2009); K. J. Yuan and A. D. Bandrauk, Phys. Rev. A **80**, 053404 (2009).
[38] D. A. Horner, S. Miyabe, T. N. Rescigno, C. W. McCurdy, F. Morales, and F. Martín, Phys. Rev. Lett. **101**, 183002 (2008).
[39] M. Walter and J. Briggs, J. Phys. B **32**, 2487 (1999).
[40] L. Nagy, S. Borbély, and K. Póra, Phys. Lett. A **327**, 481 (2004).
[41] A. Staudte, S. Patchkovskii, D. Pavičić, H. Akagi, O. Smirnova, D. Zeidler, M. Meckel, D. M. Villeneuve, R. Dörner, M. Y. Ivanov, and P. B. Corkum, Phys. Rev. Lett. **102**, 033004 (2009).